

SoraNav: Adaptive UAV Task-Centric Navigation via Zero-shot VLM Reasoning

Hongyu Song, Rishabh Dev Yadav, Cheng Guo, and Wei Pan

Abstract—Autonomous navigation under natural language instructions represents a crucial step toward embodied intelligence, enabling complex task execution in environments ranging from industrial facilities to domestic spaces. However, language-driven 3D navigation for Unmanned Aerial Vehicles (UAVs) requires precise spatial reasoning, a capability inherently lacking in current zero-shot Vision-Language Models (VLMs) which often generate ambiguous outputs and cannot guarantee geometric feasibility. Furthermore, existing Vision-Language Navigation (VLN) methods are predominantly tailored for 2.5D ground robots, rendering them unable to generalize to the unconstrained 3D spatial reasoning required for aerial tasks in small-scale, cluttered environments. In this paper, we present SoraNav, a novel framework enabling zero-shot VLM reasoning for UAV task-centric navigation. To address the spatial-semantic gap, we introduce Multi-modal Visual Annotation (MVA), which encodes 3D geometric priors directly into the VLM’s 2D visual input. To mitigate hallucinated or infeasible commands, we propose an Adaptive Decision Making (ADM) strategy that validates VLM proposals against exploration history, seamlessly switching to geometry-based exploration to avoid dead-ends and redundant revisits. Deployed on a custom PX4-based micro-UAV, SoraNav demonstrates robust real-world performance. Quantitative results show our approach significantly outperforms state-of-the-art baselines, increasing Success Rate (SR) by 25.7% and navigation efficiency (SPL) by 17.3% in 2.5D scenarios, and achieving improvements of 39.3% (SR) and 24.7% (SPL) in complex 3D scenarios.

Index Terms—Machine Learning for Robot Control; AI-Based Methods; Deep Learning for Visual Perception

I. INTRODUCTION

Autonomous navigation guided by natural language instructions represents a key capability for embodied intelligence, enabling complex task execution in environments ranging from industrial facilities to domestic spaces. In navigation tasks, this requires reasoning over 3D environments [1] while aligning actions with high-level task descriptions [2], with applications spanning industrial inspection [3], assistive navigation [4], and search-and-rescue [5]. The problem is especially challenging for UAVs operating in small-scale 3D environments, where tight endurance constraints preclude the exhaustive exploration typical of classical methods.

Existing approaches—classical mapping [6], [7], end-to-end learning [8], [9], and modular pipelines [10], [11]—each lack either language grounding, generalization, or scalable reasoning, limiting instruction-driven 3D navigation (cf. Section II).

Furthermore, existing VLN research has yet to address small-scale UAV navigation. Most work targets ground robots [9],

The authors are with the Department of Computer Science, The University of Manchester, United Kingdom (emails: {hongyu.song-3, rishabh.yadav, cheng.guo-5}@postgrad.manchester.ac.uk; wei.pan@manchester.ac.uk).

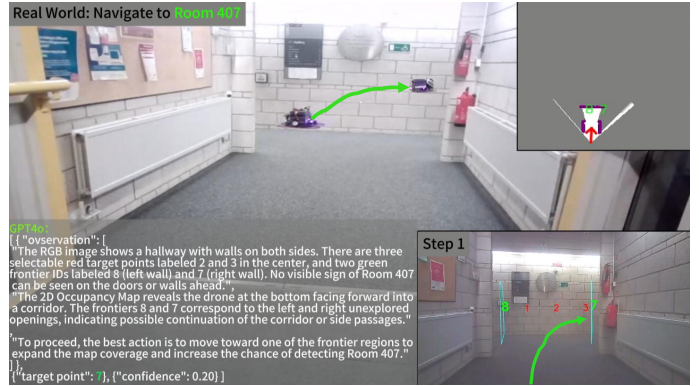


Fig. 1: Depiction of a single-step navigation process. The VLM directs the UAV toward Frontier 7 to reveal more unknown areas.

whose navigation policies do not generalize to aerial tasks requiring full 3D spatial reasoning. Prior UAV-VLN studies [12] mainly address long-range navigation from high-altitude views, which suits city-scale monitoring but not small-scale industrial or domestic environments such as factories or small parks.

The recent emergence of large VLMs like GPT [13] and Claude [14] offers a promising alternative. Their powerful zero-shot semantic reasoning capabilities make it feasible to pursue **Zero-shot VLM-guided Task-Centric Navigation (ZSVTN)**: a navigation paradigm where a robot progressively explores and reaches a target described only by a natural language and visual instruction, without task-specific fine-tuning or reliance on rich semantic priors. Here, *zero-shot* refers to the absence of any task-specific training or weight adaptation; a fixed, navigation-oriented prompt schema is used to structure the VLM query and output, but the model weights remain frozen throughout. However, general-purpose VLMs are not designed for navigation as they lack spatial grounding, generate ambiguous outputs, and cannot guarantee geometric feasibility. These limitations motivate a hybrid framework that couples VLM reasoning with geometry-aware decision-making for robust 3D UAV navigation in small-scale environments.

In this paper, we address these challenges by adopting an adaptive strategy inspired by human navigation behavior. Humans tend to move toward visible targets, explore nearby unknown areas when targets are not in sight, and avoid redundant revisits. Their decisions often rely on visual cues (e.g., doorways or intersections) as implicit waypoints, rather than explicit coordinates. Motivated by these insights, we present **SoraNav**, an adaptive navigation framework for small-scale UAVs that fuses zero-shot VLM reasoning with geometry-

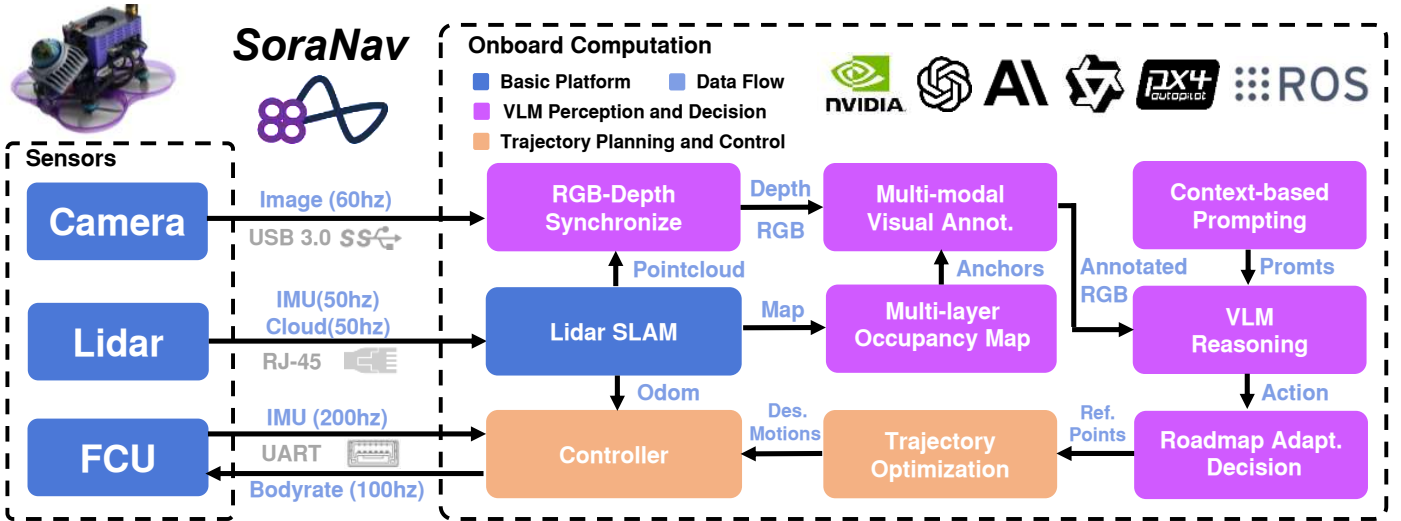


Fig. 2: Illustration of the System Overview and Data Flow.

consistent decision making, as illustrated in Figure 1 and Figure 2. Our contributions are summarized as follows:

- **Multi-modal Visual Annotation (MVA):** Geometric priors encoded as image annotations bridge VLMs’ semantic strength with spatial grounding, reducing open-ended spatial inference to structured selection among three anchor types (target, frontier, and inter-layer).
- **Adaptive Decision Making (ADM):** A hybrid switching strategy evaluates past navigation history to alternate between VLM reasoning and geometry-based exploration, avoiding dead-ends and redundant revisits.
- **Hardware–Software Platform:** A PX4-based digital twin and a real micro-UAV setup are provided for ZSVTN, to be released as open source upon acceptance.

II. RELATED WORKS

Existing autonomous navigation methods fall into three categories. Classical methods [6], [15], [16] rely on SLAM and frontier-based exploration to build geometric maps but cannot interpret language-specified goals. End-to-end approaches [8], [9], [17] learn direct visual-to-action mappings with implicit semantic grounding, yet require extensive supervision and generalize poorly. Modular pipelines [10], [11], [18] integrate VLMs for language grounding with classical planners but still depend on multiple models, handcrafted strategies, and predefined labels. Collectively, these paradigms struggle to support instruction-driven 3D navigation in unstructured environments.

Most VLN studies [8], [9], [11] assume ground-robot simulators (e.g., Habitat) with 2.5D motion and are difficult to transfer to aerial platforms due to differences in dynamics and perception. Recent UAV-VLN efforts [12], [19] target large-scale urban scenes with loose success thresholds (e.g., 20 m), unsuitable for small-scale cluttered environments requiring precise short-horizon reasoning. This gap motivates a UAV-VLN framework tailored to compact 3D spaces with instruction-driven navigation.

Large VLMs possess rich common sense knowledge, enabling them to perform scene understanding, object recognition, and even reasoning over navigation tasks, which makes ZSVTN feasible. In 2D navigation, [20], [21] propose to annotate images with candidate targets and let the VLM select the most relevant one; experiments show that their annotated representations guide decision-making more effectively than raw images. However, these methods sample waypoints uniformly without geometric priors, lack validation of VLM decisions, and are restricted to 2D settings. In 3D navigation, [12], [19] utilize VLMs to infer spatial waypoints as navigation targets in real-world UAV scenarios, but due to hallucinations [22] and a lack of explicit spatial scale awareness, VLMs can generate unsafe or unreasonable commands when reasoning from visual inputs alone. To address these gaps, SoraNav derives anchors from occupancy-based geometry with traversability guarantees instead of uniform sampling, assigns action semantics (approach, explore, switch layer) to each anchor, and validates VLM choices against exploration history via ADM.

III. PROBLEM DEFINITION

We consider **ZSVTN** in unknown environments: a UAV progressively explores and reaches a target described only by natural language instructions, using a pre-trained VLM whose weights remain frozen. We formulate this as a *goal-conditioned sequential decision problem*. The task is specified by a context-based prompt \mathcal{P} encoding the goal and behavioral constraints (Section V). At each step k , the agent maintains an information state

$$s_k = ({}^G p_k, o_k, \mathcal{V}_{1:k-1}^{\text{rm}}), \quad (1)$$

where ${}^G p_k$ is the drone pose in the global frame, o_k denotes the perceptual observation (e.g., RGB image, occupancy map), and $\mathcal{V}_{1:k-1}^{\text{rm}}$ is the set of previously visited roadmap vertices summarizing the exploration history. Given s_k and \mathcal{P} , the high-level policy

$$a_k \sim \pi(\cdot | s_k, \mathcal{P}) \quad (2)$$

selects a spatial anchor (Sections IV–V) mapped to a goal pose ${}^G p_k^{\text{goal}}$. This perception–decision–execution loop repeats until the target is visually confirmed. The policy π is realised by the VLM via adaptive decision-making combining semantic reasoning with geometry-aware exploration (Section V), rather than explicit reward optimisation.

IV. MULTI-MODAL VISUAL ANNOTATION

Since a VLM cannot directly infer geometric scales or frontier-related information from raw RGB images, we propose a **Multi-modal Visual Annotation (MVA)** scheme to encode such information. MVA derives anchors from real-time occupancy maps with traversability guarantees rather than uniform sampling. Each anchor carries an action semantic (approach, explore, or switch layer), so the VLM selects both an action type and a goal. Every decision is further validated against exploration history via ADM to filter revisits. The observation is $o_k^{\text{mva}} = (i_k^{\text{mva}}, m_k^h)$, where i_k^{mva} is the original RGB frame i_k annotated by spatial guiding anchors, and m_k^h is the 2D frontier map corresponding to the current flight altitude layer h . These annotations reveal traversability, unknown-space layout, and vertical navigability directly from a first-person view. An illustration of the anchors and visual annotation is shown in Figure 3.

A. Depth Alignment

To ensure that the anchors selected by the VLM from the RGB image correspond to precise spatial locations, we align LiDAR point clouds with RGB frames via extrinsic–intrinsic projection, thereby combining geometric accuracy with semantic perception. Let ${}^B T_C$ and ${}^B T_{\text{lidar}}$ denote the camera and LiDAR poses in the body frame B , and ${}^G T_B$ the body pose in the global frame G . A LiDAR point ${}^G p_{\text{lidar}}$ is transformed into the camera frame C as

$${}^C p_{\text{lidar}} = ({}^B T_C)^{-1} ({}^G T_B)^{-1} {}^G p_{\text{lidar}}. \quad (3)$$

The resulting point ${}^C p_{\text{lidar}} = ({}^C X, {}^C Y, {}^C Z)$ is projected onto the image plane via the pinhole model [23]: $u = f_x {}^C X / {}^C Z + c_x$, $v = f_y {}^C Y / {}^C Z + c_y$, with depth $D(u, v) = {}^C Z$. A sliding-window integration accumulates LiDAR point clouds to maintain a real-time aligned depth map.

B. Multi-layer Occupancy Map

To reduce annotation clutter and enable the VLM to interpret traversable regions across different heights, we encode the 3D scene as a multi-layer 2D occupancy map $\mathcal{M} = \{m^h\}$ [24], where each m^h is the 2D occupancy map at height layer h . Each cell is labeled as free, occupied, or unknown via raycasting. Frontiers are incrementally updated following [6], and for simplicity only the main plane and viewpoint of each frontier in the 2D height layers are considered.

C. Spatial Guiding Anchors

1) *Frontier Anchors*: The height of each frontier plane is determined by the spacing between adjacent height layers. For a frontier cluster \mathcal{F}_c in a 2D occupancy map, we compute

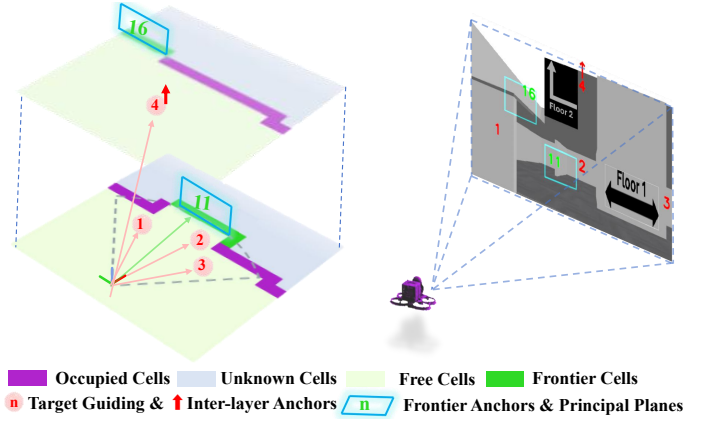


Fig. 3: Illustration of Anchors and Visual Annotations.

its principal axis \mathbf{d}_c and define the planar length as ℓ_c , if $\ell_c > \ell_{\text{max}}$, the cluster is partitioned into smaller planar segments, where ℓ_{max} denotes the maximum allowed length for a frontier cluster. Each frontier plane is approximated by four corner points $\mathbf{w}_i = ({}^G x_i, {}^G y_i, {}^G z_i)$, $i = 1, \dots, 4$ in the global frame. They are transformed into the camera frame and projected onto the image plane. Specifically, the FOV $\mathcal{F}({}^G p_k)$ is the spherical sector centered at ${}^G p_k$ with radius d_{max} and half-angle θ_{max} . If all projected corner points are inside the camera field of view, the corresponding frontier plane, defined by connecting its four corner points, is displayed on the RGB frame as an annotation. The contours of the frontier planes are shown in cyan, and their indices are labeled in green, as illustrated in Figure 3.

2) *Target Anchors*: Let $\mathcal{F}_{\text{obs}}({}^G p_k) \subset \mathcal{F}({}^G p_k)$ denote the observable frontiers within $\mathcal{F}({}^G p_k)$, with count $n_{\text{obs}}({}^G p_k)$. Given an angular span $[\varphi_L, \varphi_R]$, the *adaptive sampling cardinality* is:

$$m_\varphi = \begin{cases} m_{\text{max}}, & \text{if } n_{\text{obs}}({}^G p_k) < \tau_{\text{obs}}, \\ m_{\text{nom}}, & \text{otherwise.} \end{cases} \quad (4)$$

where τ_{obs} is the scarcity threshold, m_{nom} and m_{max} denote the nominal and maximum numbers of target directions. The discrete yaw set for target generation is then obtained via uniform discretization:

$$\Phi({}^G p_k) \triangleq \left\{ \varphi_L - \frac{l-1}{m_\varphi-1} (\varphi_L - \varphi_R) \mid l \in \{1, \dots, m_\varphi\} \right\}, \quad (5)$$

For each $\varphi \in \Phi({}^G p_k)$, we cast a ray from the sensor origin in m_k^h and select the farthest LOS-reachable point with a safety clearance from occupied or unknown cells.

3) *Inter-Layer Anchors*: During 3D navigation, the blind zones above and below the UAV increase the collision risk during altitude adjustments. To mitigate this, we introduce Inter-Layer Anchors, which are activated when collision-free navigation paths exist between adjacent height layers (e.g., they remain inactive if a ceiling is present above the UAV).

V. ADAPTIVE DECISION MAKING & TRAJECTORY PLANNING

To enable effective navigation under VLM reasoning, we propose an **Adaptive Decision Making (ADM)** mechanism.

Based on the MVA module, multi-modal prompting is first performed to obtain semantic proposals from the VLM. The prompting results are then validated by the Roadmap Adaptive Decision process, which determines whether to follow the VLM's suggestion or navigate toward nearby unexplored regions for re-prompting. The final decision is converted into waypoints for trajectory generation and subsequent control commands. An overview of the ADM pipeline is illustrated in Figure 4.

A. Multi-modal Prompting

1) *Context-Based Prompt*: Inspired by [25], we design a structured context-based prompt $\mathcal{P} = \{RG, OI, IG, BO, OS\}$ for querying the VLM. Specifically, *RG* (Role and Goal) defines the operational role and mission objective; *OI* (Observation Input) specifies the components of o_k^{mva} and instructs the VLM on their interpretation; *IG* (Important Guidelines) encodes task-specific constraints for prioritizing MVA; *BO* (Behavior Options) defines permissible actions, i.e., selecting a target g_k or a yaw adjustment $\Delta\psi_k$; and *OS* (Output Schema) specifies the structured output format for downstream processing.

2) *Prompting the VLM*: The VLM is queried with observation o_k^{mva} and prompt \mathcal{P} :

$$(o_k^{\text{intp}}, a_k^{\text{ref}}, c_{\text{det}}) = \text{VLM}(o_k^{\text{mva}} | \mathcal{P}) \quad (6)$$

where o_k^{intp} is the VLM's interpretation, a_k^{ref} the proposed action, and $c_{\text{det}} \in (0, 1)$ the detection confidence, clipped as $\tilde{c}_{\text{det}} = \text{clip}(c_{\text{det}}, \varepsilon, 1 - \varepsilon)$ with $\varepsilon = 10^{-2}$.

B. Roadmap Adaptive Decision

1) *Hypergraph Formulation*: We define the hypergraph space $\mathcal{H} = (\mathcal{V}^{\text{rm}}, \mathcal{E})$, where \mathcal{V}^{rm} is the set of *Roadmap Vertices* that encode full decision states, and \mathcal{E} is the set of decision-driven hyperedges. Each hyperedge $e_k \in \mathcal{E}$ encapsulates the k -th decision step, linking the current Roadmap Vertex v_k^{rm} to its candidates originating from different sources:

$$e_k = (v_{k-1}^{\text{rm}}, v_k^{\text{rm}}, \{v_k^{\text{vlm}}, v_k^{\text{geo}}\}) \quad (7)$$

Here v_k^{rm} is the roadmap vertex at step k , $v_k^{\text{vlm}} \in \mathcal{C}_k^{\text{vlm}}$ is the VLM-proposed candidate via MVA, and $v_k^{\text{geo}} \in \mathcal{C}_k^{\text{geo}}$ is the geometry-based candidate [26]. Each vertex stores its global position and the derived yaw.

2) *Candidate Validation*: For each step k , the informativeness of a VLM-proposed candidate v_k^{vlm} is quantified by comparing its raycast observations with the historical FOV coverage.

Instead of all historical vertices, we only consider the K nearest visited Roadmap Vertices to v_k^{vlm} , denoted by $\mathcal{N}_K(v_k^{\text{vlm}}) \subset \mathcal{V}_{1:k-1}^{\text{rm}}$. The local past coverage is

$$\mathcal{F}_{\text{past}}(v_k^{\text{vlm}}) \triangleq \bigcup_{v_j \in \mathcal{N}_K(v_k^{\text{vlm}})} \mathcal{F}(v_j), \quad (8)$$

Let $\text{Occ} : m^h \rightarrow \{-1, 0, 1\}$ denote the occupancy (-1 : unknown, 0 : free, 1 : occupied). For each azimuth θ_m sampled

within $\mathcal{F}(Gp_k)$, the discrete ray generated by Bresenham's algorithm [27] from Gp_k along $\mathbf{d}_m = [\cos \theta_m, \sin \theta_m]^\top$ is

$$\mathcal{R}(v_k^{\text{vlm}}, \theta_m) \triangleq \{g_\ell \in \mathbb{G} \mid \ell \in \mathbb{N}^+\}, \quad (9)$$

and the *hit point* is the first non-free cell encountered:

$$h_k^m = \text{center}(g_{\ell^*}), \quad \ell^* = \min\{\ell \mid \text{Occ}(g_\ell) \in \{-1, 1\}\}. \quad (10)$$

The full hit-point set at step k is $\mathcal{H}_k = \{h_k^1, \dots, h_k^{M_k}\}$.

Let $s_k^m \in \{0, 1\}$ denote the binary visibility indicator of h_k^m , defined as

$$s_k^m \triangleq \max_{v_j \in \mathcal{N}_K(v_k^{\text{vlm}})} \mathbb{1}(h_k^m \in \mathcal{F}(v_j)), \quad (11)$$

where $\mathbb{1}(\cdot)$ is the indicator function. The information gain at v_k^{vlm} is

$$G(v_k^{\text{vlm}}) \triangleq \frac{1}{M_k} \sum_{h_k^m \in \mathcal{H}_k} (1 - s_k^m), \quad (12)$$

which measures the proportion of newly observed hit points. We map the gain to a confidence score via a logistic function:

$$P_G(v_k^{\text{vlm}}) \triangleq \sigma(\alpha(G(v_k^{\text{vlm}}) - \tau_G)), \quad (13)$$

where $\sigma(x) = (1 + e^{-x})^{-1}$, $\text{logit}(p) = \log \frac{p}{1-p}$, $\alpha > 0$ controls the slope, and τ_G is the gain threshold. The validation probability is computed via log-odds fusion [28]:

$$P_{\text{valid}}(v_k^{\text{vlm}}) = \sigma(\text{logit}(P_G(v_k^{\text{vlm}})) + \lambda \text{logit}(\tilde{c}_{\text{det}})), \quad (14)$$

where $\lambda > 0$ weights the detection confidence relative to the geometric gain, and both terms are fused additively in the log-odds domain to filter out uninformative candidates. The target goal pose Gp_k^{goal} is computed from the selected anchor a_k as

$$Gp_k^{\text{goal}} = \mathcal{P}(a_k), \quad a_k = \begin{cases} v_k^{\text{vlm}}, & \text{if } P_{\text{valid}}(v_k^{\text{vlm}}) > \tau_{\text{valid}}, \\ v_k^{\text{geo}}, & \text{otherwise.} \end{cases} \quad (15)$$

where $\mathcal{P}(\cdot)$ maps the selected hypergraph node to its spatial pose and τ_{valid} is the validity threshold. The geometric fallback is also triggered when v_k^{vlm} refers to a non-existent or infeasible anchor. The final yaw of Gp_k^{goal} is set to ψ_k when $\tilde{c}_{\text{det}} > \tau_{\text{yaw}}$ and $|\psi_{\text{traj}} - \psi_k| > \tau_{\Delta\psi}$, and to the trajectory heading ψ_{traj} otherwise.

C. Trajectory Generation

To ensure that the decisions generated by the large VLM can be accurately executed, the UAV navigates toward the target goal pose Gp_k^{goal} considering both efficiency and safety. Given the current pose Gp_k , if Gp_k^{goal} originates from target anchors, a minimum-jerk trajectory is adopted, which is initialized by sampling along the straight line connecting Gp_k^{goal} and Gp_k . If it originates from frontier anchors, inter-layer anchors, or the geometry-based strategy, a trajectory generated following [29] is employed instead. The generated trajectory is then tracked by a controller through body-rate control.

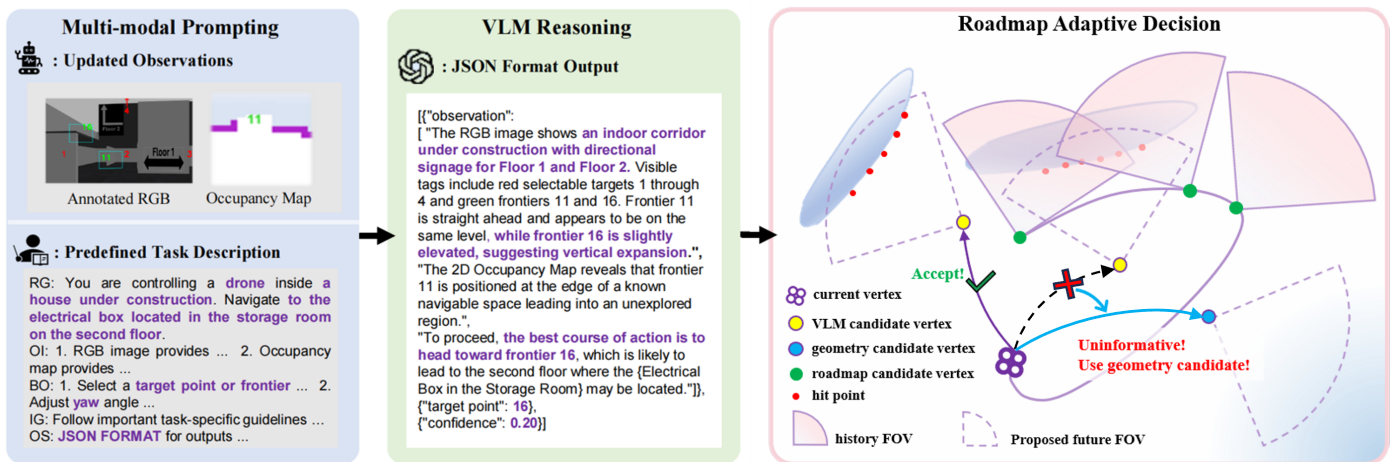
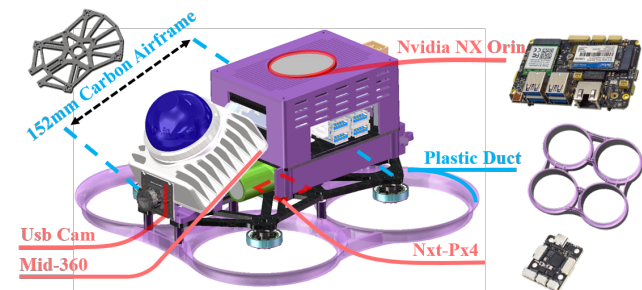
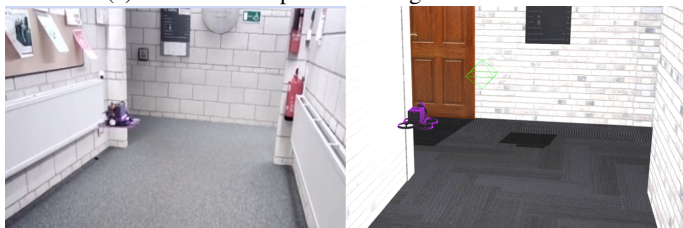


Fig. 4: **Pipeline of Adaptive Decision Making.** Multi-modal prompting guides the VLM in reasoning and decision generation. A roadmap hypergraph validates VLM decisions, enabling a transition from *uninformative* decisions to *geometric* strategies.



(a) Custom UAV platform designed for ZSVTN.



(b) Real-world (left) and simulated (right) flight scenes.

Fig. 5: UAV platform and digital twin environment.

VI. UAV PLATFORM AND DIGITAL TWIN

A high-fidelity digital twin of the UAV is developed using PX4 SITL, ROS and livox-gazebo-plugin, enabling seamless transfer of the onboard software stack between simulation and the physical drone. Figure 5b illustrates an example of the matched real and simulated environments.

To support the ZSVTN task in compact 3D environments, we designed a custom Micro Aerial Vehicle (MAV) inspired by the architecture of [30]. The platform features a compact 152 mm diagonal span to ensure agile obstacle-aware navigation in narrow spaces, shown in Figure 5a. A Mid-360 LiDAR is mounted with a fixed tilt angle to enhance vertical field-of-view coverage, enabling robust real-time localization and mapping via [31], while preserving a low-profile form factor. An Orin NX is integrated to handle perception, mapping, and trajectory control onboard, while VLM inference is offloaded to the cloud.

	Method	SR \uparrow	DtG \downarrow	NRE ($\gamma=0.5$) \downarrow
2.5D	Ours	0.83	1.62	0.65
	NavVLM	0.67	2.62	0.74
	CONVOI	0.33	3.38	0.83
	Spatial	0.22	6.03	0.95
3D	Pivot	0.00	6.69	1.00
	Ours	0.67	2.80	0.84
	Spatial	0.00	7.24	1.00

TABLE I: Image Spatial Reasoning.

VII. RESULTS AND EVALUATIONS

We conducted experiments to assess each SoraNav component and validate its sim-to-real transfer, organized along four complementary objectives: (1) how MVA enhances spatial reasoning from single-image interpretation; (2) how ADM affects the short- and long-horizon navigation performance; (3) generalizability across different VLMs; and (4) overall system performance through real-world deployment on a real UAV.

A. Experimental Setup

a) Evaluation Scenarios: We evaluate across four settings: (1) image spatial reasoning using 6 outdoor and 2 indoor 2.5D scenes plus 3 outdoor and 1 indoor 3D scenes; (2) navigation tasks comprising 4 short-horizon (2 in 2.5D, 2 in 3D) and 2 long-horizon (1 in 2.5D, 1 in 3D) scenarios; (3) model generalization across four VLMs (GPT-4o, Sonnet4, Qwen2.5, Gemini2.5); (4) real-world transfer with deployment on a physical UAV.

b) Evaluation Metrics: For Image Spatial Reasoning, we report **Success Rate (SR)**, **Distance to Goal (DtG, m)**, and **Normalized Residual Error (NRE)**, defined as $NRE = \frac{1}{N} \sum_{i=1}^N ((1 - S_i) + S_i \cdot (D_i/D_{max})^\gamma)$, where $S_i \in \{0,1\}$ indicates whether the decision succeeds, D_i denotes the spatial distance between the VLM-predicted position and the ideal target location, and D_{max} is the maximum allowable error in successful cases. This metric captures both success and decision accuracy simultaneously.

For navigation, we report SR, **Success weighted by inverse Path Length (SPL)**, and DtG, where SPL evaluates efficiency

Env & Dims	Method	Prompts ↓				Path Length ↓				DtG ↓				OR ↑	SR ↑	SPL ↑
		Avg	Std	Max	Min	Avg	Std	Max	Min	Avg	Std	Max	Min			
Warehouse 2.5D	Ours	1.14	0.35	2	1	8.10	1.31	11.02	6.72	1.93	0.35	2.30	1.11	0.86	0.86	0.67
	Spatial	2.86	0.35	3	2	4.78	2.51	7.30	0.02	4.62	2.13	8.74	2.41	1.00	0.29	0.24
	CONVOI	2.43	0.54	3	2	7.66	0.94	8.99	6.63	2.06	0.59	2.64	1.30	1.00	0.71	0.65
	NavVLM	2.43	0.54	3	2	9.95	0.04	10.00	9.91	1.42	0.03	1.44	1.39	–	–	–
	Pivot	2.57	0.54	3	2	6.95	2.05	9.48	3.75	3.53	1.84	6.86	1.56	–	–	–
Park 2.5D	Ours	1.57	0.98	3	1	9.23	3.01	15.78	7.32	2.87	0.53	3.67	2.35	1.00	0.71	0.39
	Spatial	2.86	0.35	3	2	7.94	1.16	9.90	6.04	4.35	1.31	6.18	2.63	1.00	0.14	0.07
	CONVOI	2.71	0.54	3	2	13.32	7.61	28.29	6.48	4.11	2.92	9.80	1.58	0.67	0.43	0.14
	NavVLM	3.00	0.00	3	3	6.32	2.05	10.58	5.13	5.76	0.41	6.02	4.90	–	–	–
	Pivot	3.00	0.35	3	3	9.59	4.80	18.18	4.73	5.43	3.20	11.34	1.42	–	–	–
Warehouse 3D	Ours	2.29	1.89	5	1	12.91	8.15	26.63	7.20	4.50	3.28	9.31	2.13	0.80	0.57	0.18
	Spatial	5.00	0.00	5	5	7.36	2.10	10.94	3.77	5.96	2.71	8.34	3.05	–	–	–
Park 3D	Ours	2.14	2.07	5	1	14.13	6.14	24.67	9.36	3.59	4.32	11.85	1.27	1.00	0.71	0.56
	Spatial	4.14	0.98	5	3	11.78	2.06	14.35	9.50	2.75	0.78	3.65	1.45	0.75	0.43	0.31
Kilburn 2.5D	Ours	5.67	0.47	6	5	30.55	1.91	32.38	27.92	3.16	1.32	4.96	1.83	1.00	0.67	0.58
	Spatial	6.33	1.70	8	4	8.94	2.62	12.21	5.81	11.99	0.20	12.27	11.80	–	–	–
	CONVOI	12.00	4.24	15	6	21.29	11.58	37.45	10.96	14.11	2.08	16.59	11.51	–	–	–
	NavVLM	9.67	1.70	12	8	22.46	7.41	28.98	12.09	6.83	5.43	14.51	2.93	1.00	0.33	0.33
	Pivot	15.00	0.00	15	15	22.40	11.22	37.99	12.09	12.41	6.40	19.00	3.74	–	–	–
Construction 3D	Ours	6.00	0.82	7	5	32.46	6.31	41.38	27.90	4.75	2.42	8.11	2.50	1.00	0.33	0.31
	Spatial	9.33	4.03	15	6	27.99	11.10	41.98	14.83	8.55	2.50	10.35	5.02	–	–	–

TABLE II: Short-term and Long-term Navigation. Warehouse and Park correspond to short-term tasks, while the remaining scenarios represent long-term tasks. Note that we only bold the key metrics that effectively reflect task completion.

Env & Dims	Model	Prompts ↓				Path Length ↓				DtG ↓				OR ↑	SR ↑	SPL ↑
		Avg	Std	Max	Min	Avg	Std	Max	Min	Avg	Std	Max	Min			
Kilburn 2.5D	GPT-4o	5.67	0.47	6	5	30.55	1.91	32.38	27.92	3.16	1.32	4.96	1.83	1.00	0.67	0.58
	Sonnet4	7.67	0.94	9	7	29.74	6.96	36.49	20.17	7.89	4.80	12.64	1.32	0.00	–	–
	Qwen2.5	6.00	4.24	9	0	16.59	5.59	23.94	10.39	14.78	3.17	18.97	11.30	–	–	–
	Gemini2.5	6.33	0.94	7	5	30.59	4.09	35.29	25.32	7.36	4.20	11.03	1.47	1.00	0.33	0.21
	GPT-4o	2.29	1.89	5	1	12.91	8.15	26.63	7.20	4.50	3.28	9.31	2.13	0.80	0.57	0.18
Warehouse 3D	Sonnet4	3.71	1.58	5	1	18.19	6.31	30.06	10.02	3.19	2.10	6.55	1.15	0.75	0.43	0.32
	Qwen2.5	3.43	1.68	5	1	10.01	1.78	12.43	6.67	4.84	2.84	9.66	1.34	0.33	0.14	0.13
	Gemini2.5	5.00	0.00	5	5	15.29	4.08	20.92	7.33	6.61	2.61	10.15	1.90	1.00	0.14	0.09

TABLE III: Performance Across Different VLMs.

Method	Prompts ↓	DtG ↓	SR ↑	SPL ↑
Ours	5.67	3.16	0.67	0.58
Ours w/o ADM	8.33	6.21	0.33	0.23
Ours w/o MVA	8.00	10.10	–	–

TABLE IV: Ablation study on the Kilburn 2.5D scenario.

relative to the optimal path. Additionally, we record the number of VLM promptings and the path length (m) at episode termination. We also report **Observation Rate** (OR), i.e., whether the goal lies within the FOV upon first reaching the success distance. A navigation episode is considered successful if the UAV reaches within 3 m of the goal and the goal is visible. For short-term tasks, the maximum number of prompting steps is 3 in 2.5D and 5 in 3D, whereas long-term tasks allow up to 15 prompting steps. When comparing our approach across different large models, long-term tasks are restricted to a maximum of 9 prompting steps. An episode is also terminated early if a collision occurs or 3 consecutive commands are infeasible.

c) Baselines: We consider the following four ZSVTN methods. **Spatial** follows [19], where the VLM directly de-tokenizes relative spatial positions, and thus serves as a baseline in both 2.5D and 3D environments. We further adapt three ground-robot navigation methods to aerial navigation: **NavVLM** [21], **Pivot** [20], and **CONVOI** [10]. Since these three methods do not account for altitude, they are evaluated only in 2.5D environments. NavVLM outputs collision-free points sampled at fixed angular intervals, while Pivot uniformly samples navigable waypoints; in both cases, sampled waypoints are annotated with indices on the image for the VLM to select from. CONVOI samples free cells in the occupancy grid map and requires the VLM to construct a path by sequentially connecting them. All ADM parameters are fixed across every experiment: $\alpha = 8$, $\tau_G = 0.3$, $\lambda = 1.0$, $\tau_{\text{valid}} = 0.6$, and $\tau_{\text{yaw}} = 0.65$.

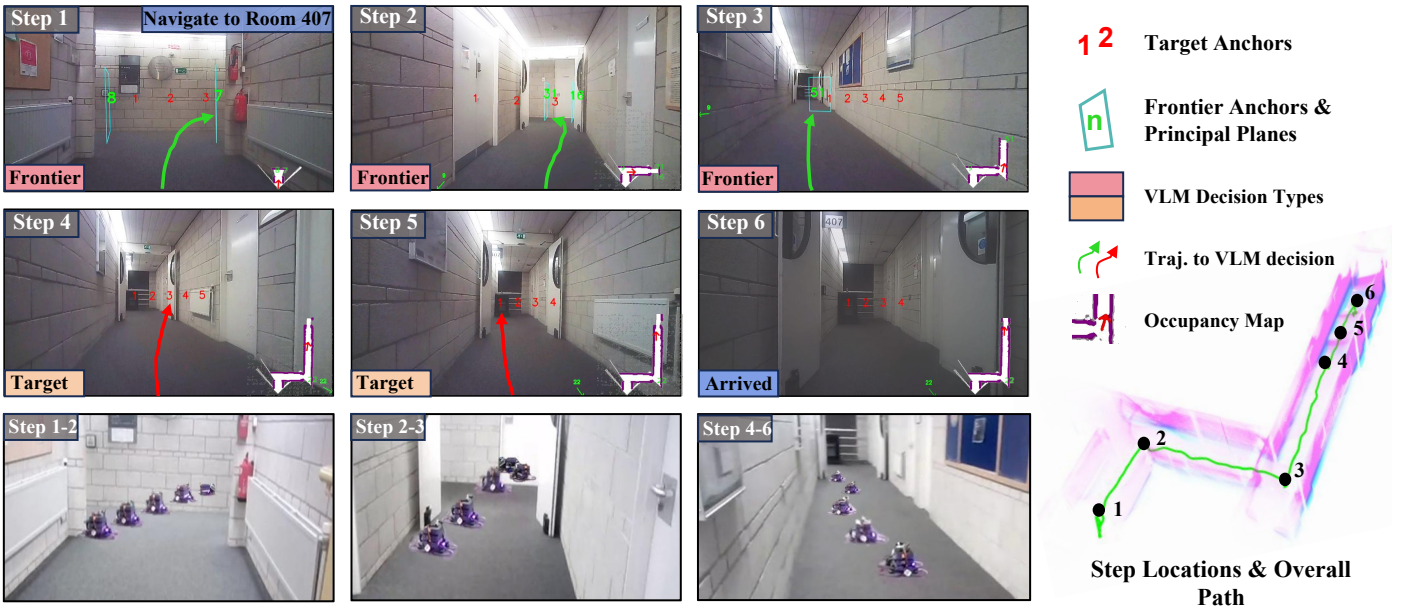


Fig. 6: Real-world Demonstration. Autonomous navigation along an indoor corridor toward Room 407.

B. Image Spatial Reasoning

This experiment evaluates the impact of MVA on the spatial decision-making capability of vision-language models (VLMs). Each method receives the same RGB input and movement range, and must select a spatial anchor based on a natural language instruction containing both explicit and implicit spatial references (e.g., “between two trees”, “near a shelf and a bin”, “right-side window on the second floor”).

Table I shows that MVA significantly improves anchor selection accuracy, achieving the highest SR and lowest DtG/NRE across both 2.5D and 3D scenes. In 2.5D, NavVLM and CONVOI perform comparably due to structured sampling, whereas Spatial underperforms in all cases, highlighting the difficulty of inferring spatial scale directly from raw images. These results confirm that MVA provides essential geometric priors that enhance spatial grounding, particularly in cluttered 3D environments.

C. Short-term and Long-term Navigation

Table II compares our method with baseline approaches across short- and long-term navigation tasks. In short-term scenarios, our approach consistently achieves the highest SR and SPL with the fewest VLM promptings. This advantage arises from the proposed Multi-modal Visual Annotation (MVA), which constrains the action space with geometric priors and adaptively refines candidate anchors, enabling more reliable decisions. Among the baselines, CONVOI performs competitively in 2.5D tasks by leveraging occupancy maps, while NavVLM obtains shortest distances to the goal but suffers from low SR due to missing yaw adjustments.

In long-term tasks, only our method and NavVLM successfully complete navigation, with our approach yielding higher SR and SPL. The longer paths arise because, when facing explored areas or infeasible decisions, our adaptive mechanism uses geometric priors to relocate the UAV for

renewed reasoning. In contrast, Spatial frequently produces infeasible commands without geometric priors, leading to early termination.

Overall, our method achieves average improvements of 25.7% (SR) and 17.3% (SPL) in 2.5D, and 39.3% (SR) and 24.7% (SPL) in 3D over the second-best method.

To further quantify each component during navigation, we conduct an ablation study on Kilburn 2.5D (Table IV). Removing either module degrades SR and SPL. Specifically, without ADM the prompt count rises and SPL drops, confirming that validation and switching effectively prevent revisits and infeasible actions. Without MVA, SR and DtG degrade to the level of Spatial, demonstrating that geometry-informed visual annotation is essential for providing the spatial scale information that VLMs lack.

D. Performance Across Different VLMs

Table III summarizes results across four VLMs. GPT-4o achieves the best overall performance in both environments (SR = 0.67/0.57, SPL = 0.58/0.18), while Sonnet4 shows competitive SPL in Warehouse 3D (0.32). Qwen2.5 and Gemini2.5 exhibit lower SR and SPL despite stable prompt usage.

E. Real-world Deployment

We deployed the proposed method on a customized UAV and successfully achieved autonomous navigation to Room 407. During the entire navigation process, the UAV interacted with GPT-4o for five prompting rounds, resulting in a total trajectory length of 26.24 m and a distance-to-goal (DtG) of 2.03 m. The doorplate of Room 407 eventually appeared within FOV. As shown in Figure 6, the VLM selected frontier anchors (green) as navigation targets in Steps 1–3, indicating relatively low confidence in recognizing Room 407 at that stage. This allowed the UAV to pass around the corridor corner and effectively explore the unknown region through single-step decisions. In

Steps 4–5, after entering the long corridor where Room 407 is located, the VLM switched to selecting target anchors (red) to approach the room.

VIII. CONCLUSION

We presented a zero-shot VLM reasoning framework for adaptive UAV task-centric navigation. By combining multimodal visual annotation with adaptive decision making, our method maps high-level language outputs into executable UAV actions and switches to geometric strategies when semantic cues are weak. The proposed method outperforms baselines in prompting efficiency, SR, and SPL, and is further validated through deployment on a real UAV.

Despite promising results, the current system reasons only at discrete stops rather than during motion. Real-world evaluation is currently limited to a single environment due to battery, safety, and flight-regulation constraints; cloud-based VLM latency is also not optimized as it depends on external API providers; extensive multi-scenario real-world trials with statistical analysis are planned as part of a journal extension. Future work will incorporate semantic priors, onboard lightweight VLMs for continuous reasoning, and scene-adaptive fine-tuning (e.g., low-rank adaptation) to further improve navigation robustness.

REFERENCES

- [1] Z. Li, H. Yu, Y. Ding, Y. Li, Y. He, and N. Akhtar, “Embodied intelligence for 3d understanding: A survey on 3d scene question answering,” *Information Fusion*, vol. 126, p. 103624, 2026. [Online]. Available: <https://www.sciencedirect.com/science/article/pii/S1566253525006967>
- [2] Y. Cui, L. Xie, Y. Zhao, J. Sun, and E. Yin, “Generating vision-language navigation instructions incorporated fine-grained alignment annotations,” 2025. [Online]. Available: <https://arxiv.org/abs/2506.08566>
- [3] L. Ren, J. Dong, S. Liu, L. Zhang, and L. Wang, “Embodied intelligence toward future smart manufacturing in the era of ai foundation model,” *IEEE/ASME Transactions on Mechatronics*, 2024.
- [4] P. Balatti, I. Ozdamar, D. Sirintuna, L. Fortini, M. Leonori, J. M. Gandarias, and A. Ajoudani, “Robot-assisted navigation for visually impaired through adaptive impedance and path planning,” 2023. [Online]. Available: <https://arxiv.org/abs/2310.14705>
- [5] H. Song, J. Yu, J. Qiu, Z. Sun, K. Lang, Q. Luo, Y. Shen, and Y. Wang, “Multi-uav disaster environment coverage planning with limited-endurance,” in *2022 International Conference on Robotics and Automation (ICRA)*. IEEE, 2022, pp. 10 760–10 766.
- [6] B. Zhou, Y. Zhang, X. Chen, and S. Shen, “Fuel: Fast uav exploration using incremental frontier structure and hierarchical planning,” 2020. [Online]. Available: <https://arxiv.org/abs/2010.11561>
- [7] Y. Zhang, X. Chen, C. Feng, B. Zhou, and S. Shen, “Falcon: Fast autonomous aerial exploration using coverage path guidance,” 2025. [Online]. Available: <https://arxiv.org/abs/2407.00577>
- [8] O. Maksymets, V. Cartillier, A. Gokaslan, E. Wijmans, W. Galuba, S. Lee, and D. Batra, “Thda: Treasure hunt data augmentation for semantic navigation,” in *Proceedings of the IEEE/CVF International Conference on Computer Vision*, 2021, pp. 15 374–15 383.
- [9] R. Ramrakhya, E. Undersander, D. Batra, and A. Das, “Habitat-web: Learning embodied object-search strategies from human demonstrations at scale,” in *Proceedings of the IEEE/CVF conference on computer vision and pattern recognition*, 2022, pp. 5173–5183.
- [10] A. J. Sathyamoorthy, K. Weerakoon, M. Elnoor, A. Zore, B. Ichter, F. Xia, J. Tan, W. Yu, and D. Manocha, “Convoi: Context-aware navigation using vision language models in outdoor and indoor environments,” 2024. [Online]. Available: <https://arxiv.org/abs/2403.15637>
- [11] N. Yokoyama, S. Ha, D. Batra, J. Wang, and B. Bucher, “Vlfn: Vision-language frontier maps for zero-shot semantic navigation,” 2023. [Online]. Available: <https://arxiv.org/abs/2312.03275>
- [12] X. Wang, D. Yang, Z. Wang, H. Kwan, J. Chen, W. Wu, H. Li, Y. Liao, and S. Liu, “Towards realistic uav vision-language navigation: Platform, benchmark, and methodology,” 2024. [Online]. Available: <https://arxiv.org/abs/2410.07087>
- [13] OpenAI, “Hello GPT-4o,” <https://openai.com/index/hello-gpt-4o/>, 2024, multimodal Large Language Model.
- [14] Anthropic, “Introducing the next generation of claude,” 2024. [Online]. Available: <https://www.anthropic.com/news/claude-3-family>
- [15] J. Roh, J. Kim, C. Park, and D. H. Shim, “Autonomous multi-floor and narrow indoor exploration using multi-criteria decision-making approach,” in *2025 22nd International Conference on Ubiquitous Robots (UR)*. IEEE, 2025, pp. 260–267.
- [16] A. Rosinol, M. Abate, Y. Chang, and L. Carlone, “Kimera: an open-source library for real-time metric-semantic localization and mapping,” in *2020 IEEE International Conference on Robotics and Automation (ICRA)*. IEEE, 2020, pp. 1689–1696.
- [17] S. Chen, T. Chabal, I. Laptev, and C. Schmid, “Object goal navigation with recursive implicit maps,” in *2023 IEEE/RSSJ International Conference on Intelligent Robots and Systems (IROS)*. IEEE, 2023, pp. 7089–7096.
- [18] M. Zhang, Y. Du, C. Wu, J. Zhou, Z. Qi, J. Ma, and B. Zhou, “Apexnav: An adaptive exploration strategy for zero-shot object navigation with target-centric semantic fusion,” 2025. [Online]. Available: <https://arxiv.org/abs/2504.14478>
- [19] Y. Gao, C. Li, Z. You, J. Liu, Z. Li, P. Chen, Q. Chen, Z. Tang, L. Wang, P. Yang, Y. Tang, Y. Tang, S. Liang, S. Zhu, Z. Xiong, Y. Su, X. Ye, J. Li, Y. Ding, D. Wang, Z. Wang, B. Zhao, and X. Li, “Openfly: A comprehensive platform for aerial vision-language navigation,” 2025. [Online]. Available: <https://arxiv.org/abs/2502.18041>
- [20] S. Nasiriany, F. Xia, W. Yu, T. Xiao, J. Liang, I. Dasgupta, A. Xie, D. Driess, A. Wahid, Z. Xu, Q. Vuong, T. Zhang, T.-W. E. Lee, K.-H. Lee, P. Xu, S. Kirmani, Y. Zhu, A. Zeng, K. Hausman, N. Heess, C. Finn, S. Levine, and B. Ichter, “Pivot: Iterative visual prompting elicits actionable knowledge for vlms,” 2024. [Online]. Available: <https://arxiv.org/abs/2402.07872>
- [21] D. Goetting, H. G. Singh, and A. Loquercio, “End-to-end navigation with vision language models: Transforming spatial reasoning into question-answering,” 2024. [Online]. Available: <https://arxiv.org/abs/2411.05755>
- [22] A. T. Kalai, O. Nachum, S. S. Vempala, and E. Zhang, “Why language models hallucinate,” 2025. [Online]. Available: <https://arxiv.org/abs/2509.04664>
- [23] R. A. Newcombe, S. Izadi, O. Hilliges, D. Molyneaux, D. Kim, A. J. Davison, P. Kohi, J. Shotton, S. Hodges, and A. Fitzgibbon, “Kinectfusion: Real-time dense surface mapping and tracking,” in *2011 10th IEEE international symposium on mixed and augmented reality*. Ieee, 2011, pp. 127–136.
- [24] P. Gonzalez, A. Mora, S. Garrido, R. Barber, and L. Moreno, “Multi-lidar mapping for scene segmentation in indoor environments for mobile robots,” *Sensors*, vol. 22, no. 10, 2022. [Online]. Available: <https://www.mdpi.com/1424-8220/22/10/3690>
- [25] X. Amatriain, “Prompt design and engineering: Introduction and advanced methods,” 2024. [Online]. Available: <https://arxiv.org/abs/2401.14423>
- [26] S. Song, D. Kim, and S. Choi, “View path planning via online multiview stereo for 3-d modeling of large-scale structures,” *IEEE Transactions on Robotics*, vol. 38, no. 1, pp. 372–390, 2021.
- [27] J. E. Bresenham, “Algorithm for computer control of a digital plotter,” *IBM Systems Journal*, vol. 4, no. 1, pp. 25–30, 1965.
- [28] A. Hornung, K. M. Wurm, M. Bennewitz, C. Stachniss, and W. Burgard, “Octomap: An efficient probabilistic 3d mapping framework based on octrees,” *Autonomous robots*, vol. 34, no. 3, pp. 189–206, 2013.
- [29] X. Zhou, Z. Wang, H. Ye, C. Xu, and F. Gao, “Ego-planner: An esdf-free gradient-based local planner for quadrotors,” *IEEE Robotics and Automation Letters*, vol. 6, no. 2, pp. 478–485, 2020.
- [30] C. Group, D. Qigeng, L. Xuchen, and A. R. X. F.H., “Cu-astro,” Video, Bilibili, September 2024, accessed: 2025-09-15. [Online]. Available: <https://www.bilibili.com/video/BV1G6HmeqEZR/>
- [31] W. Xu, Y. Cai, D. He, J. Lin, and F. Zhang, “Fast-lid2: Fast direct lidar-inertial odometry,” *arXiv preprint*, vol. 2107.06829, 2021. [Online]. Available: <https://arxiv.org/abs/2107.06829>